Bulk electronic structure of lanthanum hexaboride (LaB$_6$) by hard x-ray angle-resolved photoelectron spectroscopy

Arunothai Rattanachata,[1,2,3] Laurent C. Nicolaï [4] Henrique P. Martins [1,5] Giuseppina Conti [1,5] Matthieu J. Verstraete [6]
Mathias Gehlmann,[1,2] Shigenori Ueda [7,8] Keisuke Kobayashi,[9] Inna Vishik [1] Claus M. Schneider [1,2,10]
Charles S. Fadley [1,2,*] Alexander X. Gray [11] Ján Minár [4] and Slavomír Nemšák [5]

[1]*Department of Physics, University of California, Davis, California 95616, USA*
[2]*Materials Sciences Division, Lawrence Berkeley National Laboratory, Berkeley, California 94720, USA*
[3]*Synchrotron Light Research Institute, Nakhon Ratchasima 30000, Thailand*
[4]*New Technologies-Research Center, University of West Bohemia, 306 14 Pilsen, Czech Republic*
[5]*Advanced Light Source, Lawrence Berkeley National Laboratory, Berkeley, California 94720, USA*
[6]*Nanomat Q-MAT CESAM and European Theoretical Spectroscopy Facility, University of Liege, 4000 Liege, Belgium*
[7]*Research Center for Functional Materials, National Insititute for Materials Science, 1-1 Namiki, Tsukuba, Ibaraki 305-0044, Japan*
[8]*Synchrotron X-Ray Station at Spring-8, National Institute for Materials Science, 1-1-1 Kouto, Sayo, Hyogo 679-5148, Japan*
[9]*Quantum Beam Science Directorate, Japan Atomic Energy Agency, 1-1-1 Kouto, Sayo, Hyogo 679-5148, Japan*
[10]*Peter-Grünberg-Institut PGI-6, Forschungszentrum Jülich, 52425 Jülich, Germany*
[11]*Department of Physics, Temple University, Philadelphia, Pennsylvania 19122, USA*

In the last decade rare-earth hexaborides have been investigated for their fundamental importance in condensed matter, and for their applications in advanced technological fields. Among these compounds, LaB$_6$ has a special place, being a traditional d-band metal without additional f bands. In order to understand the bulk electronic structure of the more complex rare-earth hexaborides, in this paper we investigate the bulk electronic structure of LaB$_6$ using tender/hard x-ray photoemission spectroscopy, measuring both core-level and angle-resolved valence-band spectra. Furthermore, we compare the La $3d$ core level spectrum to cluster model calculations in order to understand the bulklike core-hole screening effects. The results show that the La $3d$ well-screened peak is at a lower binding energy compared to the main poorly screened peak; the relative intensity between these peaks depends on how strong the hybridization is between La and B atoms. We show that the recoil effect, negligible in the soft x-ray regime, becomes prominent at higher kinetic energies for lighter elements, such as boron, but is still negligible for heavy elements, such as lanthanum. In addition, we report the bulklike band structure of LaB$_6$ determined by tender/hard x-ray angle-resolved photoemission spectroscopy (HARPES). We compare HARPES experimental results to the free-electron final-state calculations and to the more precise one-step photoemission theory including matrix element and phonon excitation effects. The agreement between the features present in the experimental ARPES data and the theoretical calculations is very good. In addition, we consider the nature and the magnitude of phonon excitations in order to interpret HARPES experimental data measured at different temperatures and excitation energies. We demonstrate that the one-step theory of photoemission and HARPES experiments provides, at present, the only approach capable of probing, both experimentally and theoretically, true "bulklike" electronic band structure of rare-earth hexaborides and strongly correlated materials.

I. INTRODUCTION

Hexaboride compounds have been extensively studied in the last thirty years [1,2]. Among these compounds, lanthanum hexaboride (LaB$_6$), a thermionic material, has been studied for its high electron emissivity and very low work function of $\sim$2.5 eV for the (100) surface orientation [3]. It is one of the most widely used materials for hot cathodes in electron microscopy and lithography. Lately, it has been studied as a promising candidate for solar energy, pho-

tonic, and electronic applications [4–6]. Among the class of rare-earth hexaboride compounds, LaB$_6$ has a special place, being a traditional d-band metal without additional f bands. Other rare-earth hexaborides (RB$_6$) are investigated for their intrinsic fundamental importance in condensed matter, and for their applications in advanced technological fields [7]. For example, CeB$_6$ is a dense Kondo material that shows electric quadrupole ordering [8,9], EuB$_6$ is a ferromagnetic semimetal [10,11], YbB$_6$ is a fairly correlated Z_2 topological insulator [12]. SmB$_6$ contains additional f bands which hybridize with the d electrons to produce a narrow-gap Kondo insulator [13–16]. At present, several research groups are debating if SmB$_6$ could be also a topological Kondo insulator [17].

---

*Deceased.

However, due to the narrow band gap, the in-gap edge states near the Fermi level are very difficult to detect [18]. The theoretical prediction that SmB_6 could be a topological Kondo insulator led to renewed and intense scientific interest in the full class of rare-earth hexaborides [19].

The surface electronic structure of these materials has been widely studied both theoretically [20–23] and experimentally [6,15]. Over the past 50 years, angle-resolved photoelectron spectroscopy (ARPES) has developed into a powerful technique for determining the electronic structures of crystalline materials [24,25]. Although ARPES has played an important role in condensed-matter physics research, its capability has been limited to the characterization of surfaces, due to the short electron inelastic mean free paths (IMFPs) in solids. In a typical ARPES experiment with photon energies ranging from ~10 to 100 eV, the probing depth is about 10 Å and surface effects are dominant, in particular for rare-earth compounds with strong electron correlations.

In order to overcome this limitation, in the last decade considerable effort has been invested in the use of x-ray energies ranging from the sub-keV (soft) to multi-keV (tender/hard x-ray regime) in order to achieve higher sampling depth and to better study the properties of the bulk [26–28]. Previously, hard x-ray ARPES (HARPES) was established as a technique studying dilute magnetic semiconductors [29–31]. By using these higher excitation energies, it is possible to overcome the surface sensitivity limitations of ARPES and measure the experimental LaB_6 bulk electronic structure.

We studied LaB_6 by tender/hard x-ray photoelectron spectroscopy (XPS), measuring core levels and valence band spectra, and by hard x-ray angle-resolved photoemission spectroscopy (HARPES). Beyond being an archetypal hexaboride, LaB_6 is a very interesting case study for hard XPS because it is a stoichiometric compound with a large mass difference between heavy La (atomic weight 138.9 u) and light B (atomic weight 10.8 u). Thus, within one crystal we have two elements that will react very differently to the hard x-ray excitation: we expect to see different values of recoil energy from lanthanum and boron core levels, and different behaviors of the dispersive valence bands in HARPES due to thermal vibrations and the phonon creation and annihilation processes.

In this paper, we also demonstrate a powerful synergy between the one-step theory of photoemission and HARPES experiments in interpreting the measured data. This combination of techniques provides, at present, the only approach capable of probing, both experimentally and theoretically, true "bulklike" electronic band structure of materials

II. METHODS

The sample we investigated is a commercially available single-crystal LaB_6 (001) of 1 cm in diameter from Kimball Physics Inc. The XPS and HARPES experiments were performed at the synchrotron radiation facility SPring-8 in Hyogo Japan, at the undulator beamline BL15XU, and at the Advance Light Source (ALS) at Berkeley USA, at the bending magnet beamline BL 9.3.1. The acquisition time for the data collected at SPring-8 at the undulator beamline BL15XU presented in Fig. 6(a) was about 5 h. The acquisition time for the ARPES data collected at the bending magnet beamline 9.3.1 of the
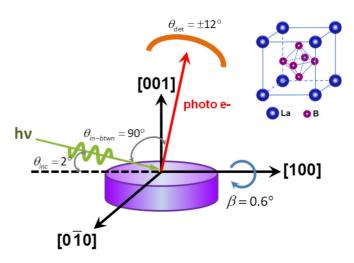

FIG. 1. Experimental geometry used at BL15XU, Spring-8. The inset shows the crystal structure of LaB_6. The crystal structure of LaB_6 is simple cubic (space group Pm-$3m$), with B_6 octahedra in body-centered positions and La atoms at the corners of the unit cell.

ALS (Fig. SM-1 of the Supplemental Material [32]) was about 5.5 h.

For the data collected at BL15XU, we used x-ray photon energies of $h\nu = 3237.5$ eV and $h\nu = 5953.4$ eV with total instrumental resolutions of 180 and 240 meV, respectively. For the data collected at BL 9.3.1, we used a photon energy of $h\nu = 2830$ eV with total instrumental resolution of about 600 meV. Figure 1 shows the experimental geometry for both experiments. The exciting radiation was incident on the sample at the grazing angle of 2.0° measured from the sample surface plane. At this grazing incident angle, the beam spot is elongated and it measures about 0.05 mm × 2.0 mm [33].

The photoemitted electrons were collected and analyzed for their kinetic energy by VG Scienta R4000 (BL15XU) and Scienta SES 2002 (BL 9.3.1) spectrometers. The sample was cooled by liquid helium down to ≈30 K at BL15XU and by liquid nitrogen down to ≈90 K at BL 9.3.1. The inset in Fig. 1 shows a schematic of a unit cell of the LaB_6 crystal structure. The binding energies were calibrated by measuring the Fermi edge and the Au $4f$ core level of an Au standard sample.

The radiation was p polarized, with the degree of linear polarization being ≈0.9 at 3237.5 eV and ≈1.0 at 5953.4 eV, with the polarization vector pointing in the direction of the analyzer. The electron takeoff angle was 88° as measured from the sample surface plane, which maximizes bulk sensitivity. This experimental geometry yields an x-ray attenuation length of 0.121 μm at 3237.5 eV and of 0.153 μm at 5953.4 eV [34], which ensures that the x-rays penetrate deep into the bulk. The information depth of the photoemission experiment, which is proportional to inelastic mean free path (IMFP) of valence electrons, was estimated using the TPP-2M formula [35]. The calculated IMFP for kinetic energies of 3237.5 and 5953.4 eV are 51.63 and 85.59 Å, respectively. Thus, the average probing depth of the valence band measurements at these two energies corresponds to about 12.4 unit cells (u.c.) and 20.6 u.c. (lattice constant $a = 4.15597$ Å) [36], respectively, providing truly bulk-sensitive measurements of the electronic properties. Previously, only studies performed in the soft x-ray

regime were reported in literature at $h\nu = 70$ eV and $h\nu = 126$ eV, corresponding to ≈ 1 and 1.4 u.c. of average probing depth [15,37]. Since tender/hard x-ray photoemission ARPES is much less sensitive to the sample surface contaminations compared to the conventional VUV ARPES, the sample was directly transferred to the analysis chamber without the need of the surface sample preparation.

In order to support the experimental data, *ab initio* calculations using the SPR-KKR [38] package were performed. This package is based on the Dirac equation thus fully accounting for relativistic effects. More specifically, the local density approximation (LDA) was used in order to derive the crystal potential. Nevertheless, a step further is required for more pertinent comparison with experimental measurements. Such theoretical calculations were obtained using the one-step model of photoemission which describes accurately the excitation process, the transport of the photoelectron to the crystal surface, as well as the escape into the vacuum as a single quantum mechanically coherent process including all multiple-scattering events. This one-step model of photoemission incorporates surface and matrix element effects and therefore allows a thorough, quantitative comparison to the experimental HARPES data. The displacements due to the final temperature were included by means of a Debye-Waller (DW) factor introduced by a coherent potential approximation (CPA) analogy [39–41]. In addition, in order to go beyond the Debye-Waller approximation, the chemical element specific phonon contributions were further taken into account by including density functional perturbation theory (DFPT) derived mean displacements [see Fig. 8(a) and Supplemental Material (SM-4) [32]]. The phonons of LaB$_6$ were calculated using DFPT [42–44] as implemented in the ABINIT software package [45]. The DFT calculations used norm conserving pseudopotentials of the ONCVPSP form from the pseudo-dojo web site [46], the GGA-PBE [47] approximation for the exchange correlation energy, a plane wave basis set cutoff of 45 Ha, and a $12 \times 12 \times 12$ grid of wave vectors for the Brillouin zone sampling of electrons and $4 \times 4 \times 4$ for the phonons. The total energy was tightly converged to 10^{-13} Ha for the ground state and 10^{-9} Ha for the phonon perturbations. The stress was relaxed to within less than 10^{-2} GPa and forces below 0.001 03 eV/Å.

The harmonic approximation was used with a fixed volume ($a = 4.155\,97$ Å): thermal expansion has a negligible effect at least up to room temperature yielding phonon dispersion relations in good agreement with the literature, as well as thermodynamic quantities, and the atomic mean square displacements (MSQD) as a function of temperature. The MSQD were incorporated in the full KKR as described above.

III. EXPERIMENTAL RESULTS

A. Chemical analysis

Figure 2 shows the survey spectra measured at photon energies of 3237.5 and 5953.4 eV. All major features are assigned to core levels (CLs) of La and B as expected. In addition, we observed C 1*s* and O 1*s* signals, which indicate some sample contamination and F 1*s* originating from a residual chamber contamination.

In order to verify whether C 1*s* and O 1*s* are contaminants on the sample surface or in the "bulk," we measured these
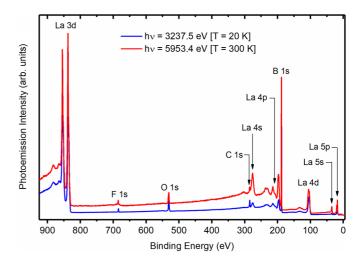

FIG. 2. Survey spectra of LaB$_6$, at 3237.5 eV (blue line) and at 5953.4 eV (red line) photon energies. The presence of O, C, and F atoms suggests surface contamination.

CLs in detail (Fig. 3) and we normalized their intensities against the La 4*s* peak. Figure 3 shows that these normalized intensities are higher in the spectrum collected at the lower photon energy (3237.5 eV) compared to that collected at higher photon energy (5953.4 eV); this is clear evidence that carbon and oxygen contamination are closer to the sample surface. The thickness of this surface contamination layer was modeled using the NIST database program Simulation of Electron Spectra for Surface Analysis (SESSA) [48]. Comparing the experimental intensities of C 1*s* and O 1*s* to those of the simulation, the thickness of this surface contamination was determined to be about 10 Å where the estimated density is 5×10^{22} atoms/cm^3. In addition, comparing the areas of the B 1*s* and La 5*p* peaks, corrected by their relative photoionization cross section, to the areas obtained by SESSA, we conclude that our LaB$_6$ sample is stoichiometric to within 3%, which lies within the expected accuracy of the XPS analysis,
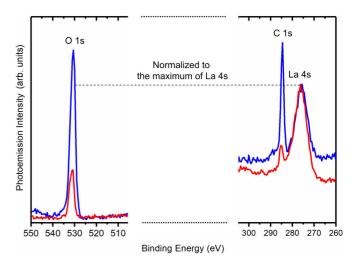

FIG. 3. Core level spectra O 1*s* and C 1*s* normalized against La 4*s* measured at photon energies, 3237.5 eV (blue line) and 5953.4 eV (red line), respectively.
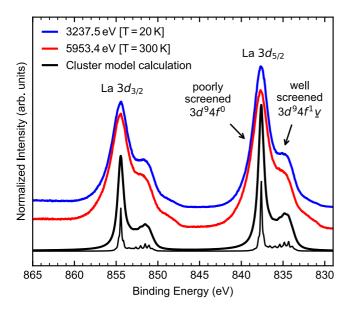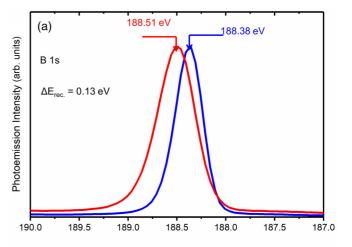
FIG. 4. La $3d$ core level photoemission spectra of LaB_6 measured at photon energies of 3237.5 eV (blue line) and 5953.4 eV (red line) compared to the calculated spectral weight of a cluster model calculation (thick black line is convoluted with a Voigt function, while the thin black line is the calculated unbroadened spectral weight). The calculated spectrum shows the final state effect of the photoemission core hole that leads to the poorly screened and well screened peaks in the experimental spectra.

using tabulated photoionization cross sections and analyzer transmission function.

The determination of the presence or absence of La and B oxidation on the surface or in the bulk is essential in order to correctly interpret the valence band and the ARPES data reported in the next sections. In literature, many studies focused on the oxidation of LaB_6 both single crystal or ceramic powder and concluded that LaB_6 in the air is highly resistant to oxidation under 1173 K [49,50]. Based on those studies, since our sample was exposed to air at room temperature, we should not observe any La or B oxidations. For this purpose, we focus our attention on B 1s and La 3d core levels.

We observed that the binding energy of the B 1s peak [Figs. 2 and 5(a)] is close to that of a pure boron compound, and that no other peaks due to possible Boron oxidation states are detected [51]. However, we noticed that the binding energy of B 1s shows a shift to higher values with higher photon excitation energies. This shift in binding energy is due to the recoil effect and will be discussed in detail later.

The experimental La 3d core levels (red and blue curves), measured at photon energies of 3237.5 and 5953.4 eV, are reported Fig. 4. The La 3d spin-orbit splitting doublet is at 837.9 eV for La $3d_{5/2}$ and at 854.8 eV for La $3d_{3/2}$; the separation between these peaks is about 17 eV in agreement with literature for nonoxidized lanthanum. Based on the B 1s [shown in Fig. 5(a) later in the paper] and La 3d binding energies we can conclude that our LaB_6 sample does not show a detectable presence of B-O_x or La-O_x in the bulk. The satellites to La $3d_{3/2}$ peak at about 848.5 and 851.5 eV are due to final state effects, as discussed in the following section.
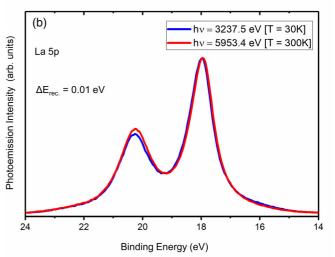

FIG. 5. XPS spectra (a) B 1s and (b) La 5p measured at photon energies, 3237.5 eV (blue line) and 5953.4 eV (red line), respectively.

B. Orbital hybridization

Since the early seventies, the doubling of each of the La $3d_{3/2}$ and La $3d_{5/2}$ peaks was extensively investigated in numerous studies of insulating [52,53] as well as metallic [54,55] compounds, and attributed to final-state screening effects [56,57]. Similar to La 3d, La 4d core levels also show such satellite structures; however, because the main La 4d spin-orbit splitting is only 2.7 eV, the satellite peaks are not as clearly resolved, and produce a more complex shape of the spectrum [58]. As a consequence, in this paper, we focus our discussion only on the La 3d region.

When interpreting core level spectra, the main peak is usually attributed to the well-screened final states, while the poorly screened satellite appears at higher binding energies. However, this general assumption is not always correct for transition metal based compounds: the satellite can also appear at lower binding energies than the main peak. In order to interpret these final-state satellites, Kotani and Toyozawa [59] proposed a model in 1974 which is still accepted today. In the ground state, the La 3d orbitals are full, and the La 4f level is empty, well above the Fermi level (E_F). In the final state of the photoemission process, the La 4f level on the

core-hole site is assumed to be pulled down below E_F because of the attractive core-hole potential. According to this mechanism, the final state splits into two configurations: one where, through hybridization, an electron near the E_F populates the $4f$ level ($3d^9 4f^1 \underline{v}$ configuration, where $\underline{v}$ denotes a hole in the valence band) and screens the core-hole potential, the other where the $4f$ level remains empty (for the duration of the photoemission event) even after its energy has been lowered below the original E_F ($3d^9 4f^0$ configuration).

In order to correctly assign the La $3d$ bands, we performed configuration interaction cluster model calculations where charge-transfer and final-state effects due to core-hole screening are included. Figure 4 shows the La $3d$ photoemission spectrum compared to cluster model calculations. The model consists of the La $3d$ core level, the La $4f$ level, and a filled valence band, and takes into account local $3d$-$4f$ electron-electron interactions and hybridization effects. The Hartree-Fock values of F^k and G^k Slater integrals that describe the atomic $4f$-$4f$ and $3d$-$4f$ electron interactions were reduced to 80% to account for bulk intra-atomic screening effects [60]. The exchange integrals and spin-orbit splitting values for the initial and final states were calculated using the COWAN code [61]. In the cluster model calculations, the $3d$-$3d$ and $4f$-$4f$ spin-orbit splittings are the same for both final states. The parameters of the model are the charge transfer energy $\Delta = E(4f^1 \underline{v}) - E(4f^0)$, the effective hybridization V_{eff} between the La $4f$ and valence band states, and the $3d$-$4f$ core-hole attractive potential U_{fc}. For the La $3d$ photoemission spectrum of LaB$_6$ these parameters were fixed to $\Delta = 11$ eV, $V_{\text{eff}} = 0.32$ eV, and $U_{\text{fc}} = 12.6$ eV. The valence band was described by a discrete set of N levels with a bandwidth of $w = 2.5$ eV; the number of N levels was increased until convergence was achieved at $N = 4$.

The calculations were performed using the QUANTY package [62] and the resulting spectral weight is obtained through a Green's function formalism. The calculated unbroadened and broadened spectral weights are shown at the bottom of Fig. 4.

The broadened curve was calculated by convoluting the spectral weight with a Voigt profile to account for experimental resolution and core-hole lifetime effects. Since Δ is relatively large and the hybridization between the valence band and the La $4f$ states is small, the calculated ground state of the system shows a mostly empty La $4f$ level, as expected, and is composed of 98.8% $4f^0$ and 1.2% $4f^1 \underline{v}$ configurations. In the final states, however, the La $4f$ states are pulled down by the core-hole potential which leads to an effective charge-transfer energy $\Delta_f = \Delta - U_{fc} = -1.6$ eV. The case where the $4f$ level remains empty, after the core hole is created, leads to the main poorly screened peak ($3d^{10}4f^0 \rightarrow 3d^9 4f^0$ transitions), whereas, if an electron near the E_F screens the core hole, it gives rise to the well-screened satellite peak dominated by $3d^{10}4f^1 \underline{v} \rightarrow 3d^9 4f^1 \underline{v}$ configuration. The negative value of Δ_f increases the contribution of well-screened $3d^9 4f^1 \underline{v}$ states in the possible final states, even if the hybridization is small. As a result, this well-screened contribution appears at a lower binding energy compared to the main poorly screened peak, as can be seen in Fig. 4. We would like to point out that the valence band has been simplified to the fully occupied B sp bands in these cluster model simulations. This simplifica-

tion reproduces very well the big screened shoulders (851.5 and 835 eV), but does not reproduce the smaller shoulders at $\sim$848.5 and $\sim$832 eV. In reality, La $5d$ has a small d-electrons count at the Fermi level that is also hybridized with the B sp bands, and these hybridized states also contribute to the core-hole screening in the final state of the photoemission process, giving rise to the satellites at $\sim$848.5 and $\sim$832 eV binding energy (BE).

The relative intensity of the La $3d$ two peaks depends on the hybridization between the La $4f$ and the valence electrons. In the case of pure La metal, the intensity of the La $3d$ well-screened peak is very small because the hybridization is almost negligible [55]. In LaB$_6$, instead, there is a small but non-negligible hybridization between La $4f$ orbitals and B sp bands. As a consequence, clear well-screened satellites ($\approx$835 and $\approx$851.5 eV) are visible in the LaB$_6$ XPS spectrum (Fig. 4).

C. Recoil effect

We have observed that the binding energy of B $1s$ corelevel increases with higher excitation energy. None of the La core levels exhibit any detectable shift, therefore the B $1s$ peak shift is not due to effects such as charging, surface oxidation, or instrumental instability, and we attribute it to the recoil effect [63,64].

The recoil effect was theoretically predicted in 1976 [65,66] but was not observed experimentally until 2007, when high brilliance third-generation synchrotron radiation sources became available for hard XPS [27]. It was observed by Takata *et al.* [67] for the C $1s$ core level of graphite and later in the valence band region for Al [68] and then for Cr and Cr$_{1-x}$Al$_x$ alloys by Boekelheide *et al.* [69] The recoil energy is negligible in traditional soft x-ray photoemission experiments, but if the kinetic energy of the emitted electron is high enough, which can occur in hard x-ray photoemission, the recoil effect becomes visible in the data.

As the photoelectron is ejected from an atom, part of the photon energy transforms into motion of the atom due to the conservation of momentum. The loss of the electron kinetic energy $E_{\text{Recoil},i}$ after ejection from an atom i can be quantified as

$$E_{\text{Recoil},i} \approx \frac{E_{\text{kin}} m_e}{M}, \quad (1)$$

where E_{kin} is the initial kinetic energy of the photoelectron, m_e is the mass of the electron, and M is the mass of the atom. The quantity $E_{\text{Recoil},i}$ is called the recoil energy. Note that Eq. (1) neglects the effect of the emitting atom being bound to a lattice.

In this work we compare the recoil effects in the LaB$_6$ core electrons at two different excitation energies $h\nu = 3237.5$ eV and $h\nu = 5953.4$ eV. LaB$_6$ is a very interesting case study for the recoil effect in hard XPS, since it consists of a heavy atom (La, atomic weight 138.9 u) and a light atom (B, atomic weight 10.8 u) in the same compound. Their recoil energies will be substantially different, much greater for B than for La. Figure 5 shows B $1s$ and La $5p$ core levels collected at those two photon energies. The B $1s$ and La $5p$ core levels did not show intrinsic peak broadening; the bandwidth variation in
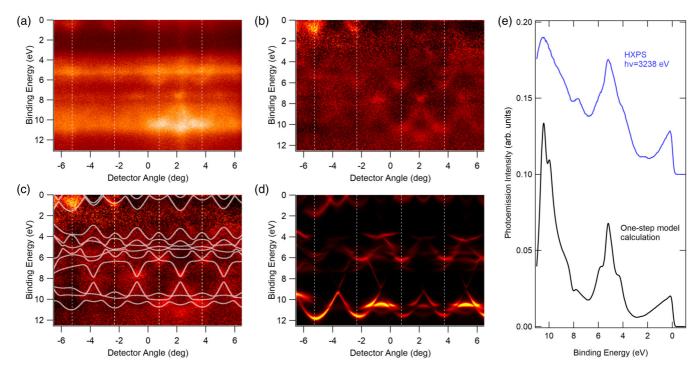
FIG. 6. (a) ARPES raw image collected at $h\nu = 3237.5$ eV and temperature 30 K; Fermi Energy is at BE = 0 eV; (b) ARPES image normalized by the density-of-states (DOS) and by the x-ray photoelectron diffraction (XPD) modulations; (c) free electron final state (FEFS) band structure calculation (gray solid lines) overlaid on the ARPES data from (b); (d) angle-resolved photoemission data calculated by the one-step theory at $h\nu = 3238$ eV and temperature 30 K; (e) experimental (HXPS at $h\nu = 3237.5$ eV, $T = 30$ K) and calculated ($h\nu = 3238$ eV, $T = 30$ K) angle-integrated valence band intensities.

B $1s$ at the two different photon energies is consistent with the corresponding total instrumental energy resolution. Shirley background was subtracted [70] from these spectra and their heights were normalized to their peak maximum.

In Fig. 5(a), a difference of 0.13 eV in the binding energies of the B $1s$ peak is observed at those two photon energies. The calculated difference using

$$\Delta E_{\text{Recoil},B} = E_{\text{Recoil},B}(5953.4 \text{ eV}) - E_{\text{Recoil},B}(3237.5 \text{ eV})$$

(2)

yields 0.14 eV for B $1s$. Figure 5(b) instead shows that La $5p_{3/2}$ does not exhibit any detectable shift, and the calculated value of $\Delta E_{\text{Recoil},La}$ is 0.01 eV, too small to be observed in our experiment.

The agreement between the experimental recoil shifts with the calculated value from Eq. (1), which is valid for emission from an isolated atom, suggests, in the first approximation, that the boron atoms can freely recoil out of the lattice during the present photoemission process. This experimental result is not in contradiction with what was calculated by Korsukova *et al.* [71], reporting that the estimated Debye temperature of LaB$_6$ is of 417 K for "the more loosely bound lanthanum ions" and 732 K for the rigid boron network. In fact, if we consider that the experimental Boron recoil energy of 0.13 eV corresponds to a temperature of $\approx$1500 K, which is well above the predicted Debye temperature ($\approx$800 K) of the boron lattice, we can conclude that B recoils as an approximately "free" atom.

The presence of core-level recoil energy shifts of various magnitudes is an important aspect in hard x-ray photoemis-

sion spectroscopy, and has to be carefully taken into account in the interpretation of the data. Furthermore, the recoil energy is intimately linked to the photon-phonon interaction and to the fraction of transitions in which the entire lattice could recoil, as described by the DW factor. Due to this interaction, the La and B dispersive valence bands will show different behavior in the HARPES data. For instance, the creation and annihilation of phonons during photoemission can cause a smearing along the momentum axis in the HARPES data, as discussed in detail below.

D. Valence-band structure

With the development of third-generation and the dawn of fourth-generation synchrotron sources [28], HARPES is now being used routinely to probe the "true" bulk properties of solids, providing greater information depth due to the large inelastic mean-free path of the escaping photoelectrons [72,73]. However, ARPES measurements in the hard x-ray regime present specific challenges due to quite low photoionization cross sections, strong phonon scattering, photoelectron diffraction effects, and large photon momentum transfer.

We report in this section HARPES applied to LaB$_6$ where, as calculated from IMFP, about 12 u.c. and about 21 u.c. are probed at excitation energy $h\nu = 3237.5$ eV and at $h\nu = 5953.4$ eV respectively.

In addition to the ARPES data collected at $h\nu = 3237.5$ eV and $T = 30$ K, shown in Fig. 6, we have collected ARPES data at $h\nu = 2830$ eV and $T \approx 90$ K as well as at $h\nu = 5953.4$ eV and $T = 300$ K. The experimental ARPES images

of these other two experiments are reported in Supplemental Material SM-1 [32].

Figure 6(a) shows the detector image of LaB_6 ARPES, measured at the photon energy of 3237.5 eV and at a temperature of 30 K. No cleaning of the atmosphere-exposed LaB_6 surface was done. Cooling the sample partly suppresses the smearing of the band structures, which is due to phonon-assisted indirect transitions. The phonon smearing can be estimated using a photoemission DW factor $W(T)$, which predicts the fraction of the direct transitions for a given photon energy and temperature calculated from

$$W(T) = \exp\left(-\frac{g_{hkl}^2}{3}\langle U^2(T)\rangle\right), \qquad (3)$$

where g_{hkl} is the magnitude of the bulk reciprocal lattice vector involved in the direct transitions for a given photon energy and $U^2(T)$ is the element-specific three dimensional mean-squared vibrational displacement for a given temperature [29,74,75].

Based on the Debye temperature, as reported in [Ref. [71]], and on Eq. (3) we estimated that the DW factor for LaB_6 is about 0.6 at 3237.5 eV and at 30 K, and as a consequence, we expect to observe a clear bulk dispersive band structure.

The detector image in Fig. 6(a) is dominated by the density of states (DOS) and by the x-ray photoelectron diffraction (XPD) modulations. The effects of DOS [Eq. (4a)] and XPD [Eq. (4b)] can be removed by normalizing this image by the integrated photoelectron intensities:

$$\text{DOS} \approx \int I(E,\vartheta)d\vartheta \qquad (4a)$$

and

$$\text{XPD} \approx \int I(E,\vartheta)dE. \qquad (4b)$$

This normalization process also removes the matrix element effects. Figure 6(b) shows the normalized enhanced angle-resolved bulk band electronic structure corrected also by the relative angular shift of the band structure features with respect to the x-ray photoelectron diffraction pattern. We calculated that this relative angular shift in our experiment is 3.219° (see Supplemental Material SM-2 [32]).

IV. THEORETICAL CALCULATIONS

A. Valence band photoemission calculations

We compared the experimental ARPES data reported in Fig. 6(b) to bulk electronic band structure calculated by DFT using free-electron final-state (FEFS) approximation and by the more accurate one-step model of photoemission, including lattice vibrations [38]. FEFS calculations using DFT generated band structures are reported in Fig. 6(c). In Supplemental Material SM-3 [32] we describe the FEFS model [76]. A particular challenge in HARPES experiments, compared to conventional low-energy ARPES, is the extreme sensitivity to the sample alignment. We found that the best agreement between experiment and calculation is given with an additional tilt of 0.6° compared to the initially assumed sample geometry (SM-3 [32]) [77]. Such a small misalignment is caused by imperfect mounting of the sample to the sample holder and
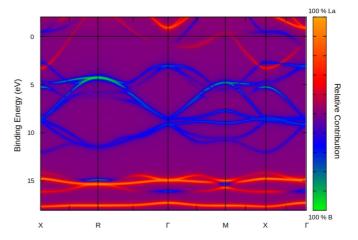

FIG. 7. Calculated Bloch spectral functions projected onto La and B sites, showing mixed character of bands throughout the valence band region.

it is to be expected. Once the optimized geometries were obtained using the FEFS model, we proceeded to simulate the HARPES spectra with the one-step photoemission model [78,79].

Unlike the FEFS calculations, the one-step calculations include the concepts of light polarization, surfaces, and final-states effects, thus allowing quantitative comparison to the experimental HARPES data. All presented calculations were performed for a La-terminated surface. Figure 6(d) shows the calculated band dispersion results from the one-step theory, with white dashed lines being guides to the eye, marking neighboring Brillouin zones. For better comparison with experimental data in Fig. 6(b) and to enhance band structure features, XPS limit was not included in spectra calculated in Fig. 6. The agreement between the features present in the experimental ARPES data and the theoretical calculations is very good. In addition, as a further more quantitative comparison between the experimental and calculated valence band photoemission spectra, we calculated angle-integrated counterparts of angle-resolved data shown in Figs. 6(a) and 6(d). These results are shown in Fig. 6(e), with all the features present in the experimental data also present in the calculated spectra, with slightly better resolution in the calculated spectra. Calculated spectra were convoluted with a 250-meV-wide Gaussian function to account for the experimental broadening.

As a next step, we calculated the theoretical projected Bloch spectral functions (BSFs) onto La and B sites along certain high symmetry orientations, as shown in Fig. 7. The BSF plot clearly shows a mixed character of bands throughout the entire valence band region. The B contribution is mostly between 5 and 12.5 eV, although La is not negligible. The La contribution, on the other hand, is mostly concentrated between 0 and 4 eV and below 12.5 eV. The character of the individual bands will be discussed with regard to phonon excitations, as described in the next section.

B. Vibrational calculations

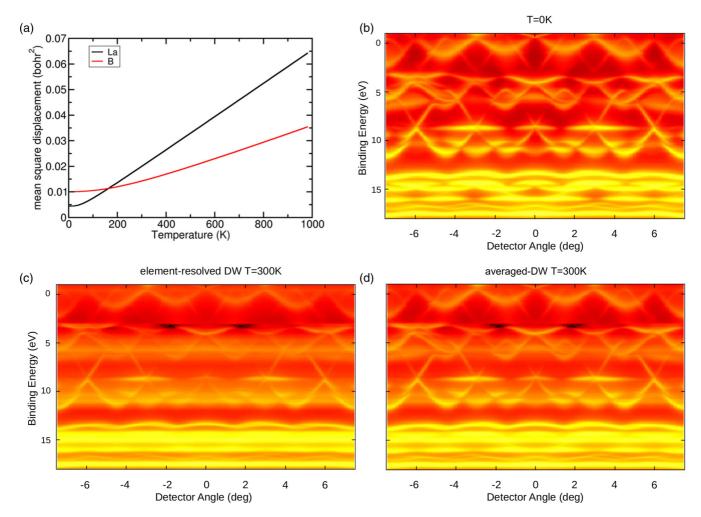Figure SM-4a [32] shows the phonon band structure of LaB_6 as calculated by DFPT (see the Methods section), with

FIG. 8. (a) Mean square displacement of the La and B atoms, as a function of temperature; (b) one-step photoemission calculations at $hv = 3238$ eV $T = 0$ K; (c), (d) one-step calculations with different implementation of phonon excitations, either element resolved (c) or averaged (d). The wave-vector blurring is noticeably different, especially for bands around 10 eV, and stronger for the element resolved case.

the element projected density of states (DOS) in the side panel. The optical manifold is completely dominated by B and separated by an energy gap from the acoustic manifold which moves only the La atom. The Debye model is inappropriate in both cases: for B the modes are rarely linear in dispersion except around 50 meV and for La much of the dispersion is flat beyond the first fifth of the Brillouin zone. Figure SM-4b shows the specific heat of LaB_6 within the harmonic approximation and DFPT, as a function of temperature. The inset shows the small bump created by the lanthanum manifold around 50 K. Figure 8(a) shows the mean square displacement of the La and B atoms, as a function of T. The light B atoms have significant zero-point motion contributions at $T = 0$ K, but increase more slowly as they have no low frequency contributions. The heavy La atoms start with a smaller zero point effect, but increase more quickly with T due to the increasing Bose-Einstein occupation of the acoustic modes. The complex phonon band structure of LaB_6 explains the contradictory values obtained for the Debye temperature fit based on calorimetric and x-ray experiments. Neither boron nor lanthanum atoms behave according to the Debye model: the full dynamics must be taken into account to calculate the MSQD at high and low temperatures.

As a final step of our analysis, we included the phonon effects in the one-step model calculations based on previously developed methodology [39–41,78]. The one-step photoemission calculations are depicted in Figs. 8(b)–8(d), showing the effects of different lattice vibrations theoretical descriptions. The DW factor is implemented with atoms considered "frozen," meaning that lattice vibrations, including zero point motion, are completely neglected [Fig. 8(b)]. When T increases, lattice vibrations are taken into account such that phonon-assisted electronic transitions are allowed. In other words, in the photoemission process, the electrons can have access to indirect transitions. Figure 8(d) shows the case of $T = 300$ K with an averaged DW factor for both chemical elements. Figure 8(c) reveals the changes in the spectrum when including species specific DW factors as derived from DFPT calculations. In addition to the ARPES data reported in Figs. 6(a) and 6(b), Fig. SM-1a [32] shows the ARPES image collected at $hv = 2830$ eV and at $T \approx 90$ K. The ARPES images reported in Figs. 6(a) and 6(b) and in Fig. SM-1a, having similar photon energy but measured at very different temperature, are dramatically different. In Fig. SM-1a the bands between 5 and 10 eV, mainly attributed to B atoms, are completely smeared out and the only visible dispersing bands

are those attributed to La close to the Fermi energy. Furthermore, the ARPES image collected at about 5953.4 eV and $T = 300$ K (Fig. SM-1b) shows that B bands have vanished and La bands are almost completely smeared out, leaving a minority of direct transitions, which can barely be extracted from the noise. As shown in Fig. 8, at 300 K, the full DFPT phonon DW factor smears the bands significantly more than expected from a simpler model.

V. CONCLUSION

A detailed characterization of the position and intensity of the XPS core level peaks of the C 1s, O 1s, and B 1s and La 3d core levels suggests that the LaB$_6$ crystal studied here does not show bulk impurities and that the carbon and oxygen contaminations are only on the top sample surface. The well-screened and poorly screened La 3d peaks were identified and interpreted by means of cluster model calculations. We determined that there is a small but non-negligible hybridization between La 4f orbitals and B sp bands producing the main poorly-screened peaks ($3d^9 4f^0$) at 838 and 854.5 eV, respectively, and the clear well-screened satellites ($3d^9 4f^1 \underline{v}$) at 835 and at 855.2 eV, respectively. In addition, using tender/hard XPS we demonstrated that, within one crystal, La and B act noticeably differently to the hard x-ray excitation. Their recoil energies are substantially different, specifically it is much larger for B than for La. Interestingly, little to no momentum is transferred to the crystal lattice and B atoms recoil as if they were free on the photoemission time scale.

We also report hard x-ray ARPES measurements for a rare-earth hexaboride compound. We have shown that the observed ARPES data can in first approximation be understood within a simple free-electron final-state model. Furthermore, one-step theory provided, at a more quantitative level, a good description of the experimental ARPES data including the relative intensities of most features. The agreement between the experimental data and the one-step model calculations is very good.

In the temperature dependence of the experimental data, there is a clear trend for the bands with boron character to broaden and vanish at increasing temperature, due to the breaking of the $\boldsymbol{k}$-conserving dipole selection rule. We model these effects with *ab initio* calculations implementing lattice vibrations within the one-step model of photoemission through the coherent potential approximation (CPA), with a qualitative agreement between the trends in experiment and theory. The complex phonon band structure of LaB$_6$ explains the contradictory values obtained for the Debye temperature fit based on calorimetric and x-ray experiments. Neither boron nor lanthanum atoms behave according to the Debye model, dictating the necessity to take into account the full dynamics in order to calculate the atomic mean square displacements (MSQD) at high and low temperatures.

Last, we demonstrated that hard x-ray excited ARPES combined with one-step theory of photoemission is a very powerful way experimentally and theoretically to determine true bulklike electronic band structure in complex materials. This successful combination of experimental and theoretical study unlocks a way of characterizing another class of materials, such as rare-earth hexaborides.

[1] M. Trenary, Surface science studies of metal hexaborides, Sci. Technol. Adv. Mater. **13**, 023002 (2012).

[2] J. T. Cahill and O. A. Graeve, Hexaborides: A review of structure, synthesis and processing, J. Mater. Res. Technol. **8**, 6321 (2019).

[3] A. N. Broers, Some experimental and estimated characteristics of the lanthanum hexaboride rod cathode electron gun, J. Phys. E: Sci. Instrum. **2**, 273 (1969).

[4] E. Sani, L. Mercatelli, M. Meucci, L. Zoli, and D. Sciti, Lanthanum hexaboride for solar energy applications, Sci. Rep. **7**, 718 (2017).

[5] X. H. Ji, Q. Y. Zhang, J. Q. Xu, and Y. M. Zhao, Rare-earth hexaborides nanostructures: Recent advances in materials, characterization and investigations of physical properties, Prog. Solid State Chem. **39**, 51 (2011).

[6] W. Wang, Y. Wang, M. Zhang, R. Wang, G. Chen, X. Chang, F. Lin, F. Wen, K. Jia, and H.-X. Wang, An enhancement-mode hydrogen-terminated diamond field-effect transistor with lanthanum hexaboride gate material, IEEE Electron Device Lett. **41**, 585 (2020).

[7] S. V. Ramankutty, N. de Jong, Y. K. Huang, B. Zwartsenberg, F. Massee, T. V. Bay, M. S. Golden, and E. Frantzeskakis, Comparative study of rare earth hexaborides using high resolution angle-resolved photoemission, J. Electron. Spectrosc. Relat. Phenom. **208**, 43 (2016).

[8] W. A. C. Erkelens, L. P. Regnault, P. Burlet, J. Rossat-Mignod, S. Kunii, and T. Kasuya, Neutron scattering study of the antiferroquadrupolar ordering in CeB$_6$ and Ce$_{0.75}$La$_{0.25}$B$_6$, J. Magn. Magn. Mater. **63**, 61 (1987).

[9] A. S. Cameron, G. Friemel, and D. S. Inosov, Multipolar phases and magnetically hidden order: Review of the heavy-fermion compound Ce$_{1-x}$La$_x$B$_6$, Rep. Prog. Phys. **79**, 066502 (2016).

[10] S. Süllow, I. Prasad, M. C. Aronson, J. L. Sarrao, Z. Fisk, D. Hristova, A. H. Lacerda, M. F. Hundley, A. Vigliante, and D. Gibbs, Structure and magnetic order of EuB$_6$, Phys. Rev. B **57**, 5860 (1998).

[11] L. Degiorgi, L. E. Felder, H. R. Ott, J. L. Sarrao, and Z. Fisk, Low-Temperature Anomalies and Ferromagnetism in EuB$_6$, Phys. Rev. Lett. **79**, 5134 (1997).

[12] J. Ying, L. Tang, F. Chen, X. Chen, and V. V. Struzhkin, Coexistence of metallic and insulating channels in compressed YbB$_6$, Phys. Rev. B **97**, 121101(R) (2018).

[13] E. Beaurepaire, J. P. Kappler, and G. Krill, X-ray-absorption near-edge structure study in mixed-valent samarium systems, Phys. Rev. B **41**, 6768 (1990).

[14] J. Demsar, V. K. Thorsmølle, J. L. Sarrao, and A. J. Taylor, Photoexcited Electron Dynamics in Kondo Insulators and Heavy Fermions, Phys. Rev. Lett. **96**, 037401 (2006).

[15] A. P. Sakhya and K. Maiti, Ground state anomalies in SmB$_6$, Sci. Rep. **10**, 1262 (2020).

[16] S.-K. Mo, G.-H. Gweon, J. D. Denlinger, H.-D. Kim, J. W. Allen, C. G. Olson, H. Hochst, J. L. Sarrao, and Z. Fisk, ARPES study of X-point band overlaps in LaB$_6$ and SmB$_6$ - Contrast to SrB$_6$ and EuB$_6$, Phys. B (Amsterdam, Neth.) **312**, 668 (2002).

[17] C.-J. Kang, J. Kim, K. Kim, J. Kang, J. D. Denlinger, and B. I. Min, Band symmetries of mixed-valence topological insulator: SmB$_6$, J. Phys. Soc. Jpn. **84**, 024722 (2015).

[18] M. Neupane, N. Alidoust, S.-Y. Xu, T. Kondo, Y. Ishida, D. J. Kim, Chang Liu, I. Belopolski, Y. J. Jo, T.-R. Chang, H.-T. Jeng, T. Durakiewicz, L. Balicas, H. Lin, A. Bansil, S. Shin, Z. Fisk, and M. Z. Hasan, Surface electronic structure of the topological Kondo-insulator candidate correlated electron system SmB$_6$, Nat. Commun. **4**, 2991 (2013).

[19] A. Arab, A. X. Gray, S. Nemšák, D. V. Evtushinsky, C. M. Schneider, D.-J. Kim, Z. Fisk, P. F. S. Rosa, T. Durakiewicz, and P. S. Riseborough, Effects of spin excitons on the surface states of SmB$_6$ A photoemission study, Phys. Rev. B **94**, 235125 (2016).

[20] P. G. Perkins, D. R. Armstrong, and A. Breeze, On the electronic structure of some metal hexaborides, J. Phys. C: Solid State Phys. **8**, 3558 (1975).

[21] S. Kimura, T. Nanba, M. Tomikawa, S. Kunii, and T. Kasuya, Electronic structure of rare-earth hexaborides, Phys. Rev. B **46**, 12196 (1992).

[22] Z. Pan, Y. Pan, J. Jiang, and L. Zhao, High-throughput electronic band structure calculations for hexaborides, in *Intelligent Computing: Proceedings of the 2019 Computing Conference* (Springer International Publishing, 2019), Vol. 2, pp. 386–395.

[23] J. A. Alarco, P. C. Talbot, and I. D. R. Mackinnon, Comparison of functionals for metal hexaboride band structure calculations, Model Numeri. Simul. Mater. Sci. **4**, 53 (2014).

[24] F. J. Himpsel, Angle-resolved measurements of the photoemission of electrons in the study of solids, Adv. Phys. **32**, 1 (1983).

[25] A. Damascelli, Z. Hussain, and Z.-X. Shen, Angle-resolved photoemission studies of the cuprate superconductors, Rev. Mod. Phys. **75**, 473 (2003).

[26] D. L. Feng, Photoemission spectroscopy: Deep into the bulk, Nat. Mater. **10**, 729 (2011).

[27] K. Kobayashi, Hard x-ray photoemission spectroscopy, Nucl. Instrum. Methods Phys. Res. A **601**, 32 (2009).

[28] C. S. Fadley and S. Nemsak, Some future perspectives in soft-and hard-X-ray photoemission, J Electron Spectros. Relat. Phenom. **195**, 409 (2014).

[29] A. X. Gray, C. Papp, S. Ueda, B. Balke, Y. Yamashita, L. Plucinski, J. Minár, J. Braun, E. R. Ylvisaker, C. M. Schneider, W. E. Pickett, H. Ebert, K. Kobayashi, and C. S. Fadley, Probing bulk electronic structure with hard X-ray angle-resolved photoemission, Nat. Mater. **10**, 759 (2011).

[30] S. Nemšák, M. Gehlmann, C.-T. Kuo, S.-C. Lin, C. Schlueter, E. Mlynczak, T.-L. Lee, L. Plucinski, H. Ebert, I. Di Marco, J. Minár, C. M. Schneider, and C. S. Fadley, Element- and momentum-resolved electronic structure of the dilute magnetic semiconductor manganese doped gallium arsenide, Nat. Commun. **9**, 3306 (2018).

[31] A. Keqi, M. Gehlmann, G. Conti, S. Nemšák, A. Rattanachata, J. Minár, L. Plucinski, J. E. Rault, J. P. Rueff, M. Scarpulla, M. Hategan, G. K. Pálsson, C. Conlon, D. Eiteneer, A. Y. Saw, A. X. Gray, K. Kobayashi, S. Ueda, O. D. Dubón, C. M. Schneider, and C. S. Fadley, Electronic structure of the dilute magnetic semiconductor Ga$_{1-x}$Mn$_x$P from hard x-ray photoelectron spectroscopy and angle-resolved photoemission, Phys. Rev. B **97**, 155149 (2018).

[32] See Supplemental Material at http://link.aps.org/supplemental/10.1103/PhysRevMaterials.5.055002 for additional ARPES data (SM-1); relative angular shift of the band structure features with respect to the x-ray photoelectron diffraction pattern (SM-2); free electron final state calculations (SM-3); phonon band structure of LaB$_6$ (SM-4).

[33] S. Ueda, Y. Katsuya, M. Tanaka, H. Yoshikawa, Y. Yamashita, S. Ishimaru, Y. Matsushita, and K. Kobayashi, Present Status of the NIMS Contract Beamline BL15XU at SPring-8, in *SRI 2009, 10th International Conference on Radiation Instrumentation*, edited by R. Garrett, I. Gentle, K. Nugent, and S. Wilkins, AIP Conf. Proc. No. 1234 (AIP, Melville, NY, 2010), pp. 403–406.

[34] B. L. Henke, E. M. Gullikson, and J. C. Davis, X-ray interactions: Photo-absorption, scattering, transmission and reflection at E = 50−30 000 eV, Z = 1-92, Atomic Data Nucl. Data Tables **54**, 181 (1993).

[35] H. Shinotsuka, S. Tanuma, C. J. Powell, and D. R. Penn, Calculations of electron inelastic mean free paths. X. Data for 41 elemental solids over the 50 eV to 200 keV range with the relativistic full Penn algorithm, Surf. Interface Anal. **47**, 871 (2015).

[36] N. N. Sirota, V. V. Novikov, V. A. Vinokurov, and Yu. B. Paderno, Temperature dependence of the heat capacity and lattice constant of lanthanum and samarium hexaborides, Phys. Solid. State **40**, 1856 (1998).

[37] A. Rattanachata, Bulk electronic structure of rare-earth hexaboride by hard x-ray angle-resolved photoemission spectroscopy, Ph.D. thesis, University of California Davis, 2021.

[38] H. Ebert, D. Koedderitzsch, and J. Minár, Calculating condensed matter properties using the KKR-Green's function method—recent developments and applications, Rep. Prog. Phys. **74**, 096501 (2011).

[39] J. Braun, J. Minár, S. Mankovsky, V. N. Strocov, N. B. Brookes, L. Plucinski, C. M.Schneider, C. S. Fadley, and H. Ebert, Exploring the XPS limit in soft and hard x-ray angle-resolved photoemission using a temperature-dependent one-step theory, Phys. Rev. B **88**, 205409 (2013).

[40] H. Ebert, S. Mankovsky, K. Chadova, S. Polesya, J. Minár, and D. Ködderitzsch, Calculating linear-response functions for finite temperatures on the basis of the alloy analogy model, Phys. Rev. B **91**, 165132 (2015).

[41] L. Nicolai and J. Minar, XPS limit in soft X-ray photoemission spectroscopy of Ag(001), in *Applied Physics of Condensed Matter (APCOM 2018)*, AIP Conf. Proc. No. 1996, edited by J. Sitek, J. Vaida, and I. Jamnicky, (AIP, Melville, NY, 2018), p. 020033.

[42] X. Gonze, First-principles responses of solids to atomic displacements and homogeneous electric fields: Implementation of a conjugate-gradient algorithm, Phys. Rev. B **55**, 10337 (1997).

[43] X. Gonze and C. Lee, Dynamical matrices, Born effective charges, dielectric permittivity tensors, and interatomic force constants from density-functional perturbation theory, Phys. Rev. B **55**, 10355 (1997).

[44] S. Baroni, S. de Gironcoli, A. Dal Corso, and P. Giannozzi, Phonons and related crystal properties from density-functional perturbation theory, Rev. Mod. Phys. **73**, 515 (2001).

[45] A. H. Romero, D. C. Allan, B. Amadon, G. Antonius, T. Applecourt, L. Baguet, J. Bieder, F. Bottin, J. Bouchet, E. Bousquet, F. Bruneval, G. Brunin, D. Caliste, M. Côté, J. Denier, C. Dreyer, P. Ghosez, M. Giantomassi, Y. Gillet, O. Gingras *et al.*, ABINIT: Overview and focus on selected capabilities, J. Chem. Phys. **152**, 124102 (2020).

[46] D. R. Hamann, Optimized norm-conserving Vanderbilt pseudopotentials, Phys. Rev. B **88**, 085117 (2013).

[47] J. P. Perdew, K. Burke, and M. Ernzerhof, Generalized Gradient Approximation Made Simple, Phys. Rev. Lett. **77**, 3865 (1996).

[48] W. Smekal, W. S. M. Werner, and C. J. Powell, Simulation of electron spectra for surface analysis (SESSA): A novel software tool for quantitative Auger-electron spectroscopy and x-ray photoelectron spectroscopy, Surf. Interface Anal. **37**, 1059 (2005).

[49] M. F. Sunding, K. Hadidi, S. Diplas, O. M. Løvvik, T. E. Norby, and A. E. Gunnæs, XPS characterisation of in situ treated lanthanum oxide and hydroxide using tailored charge referencing and peak fitting procedures, J. Electron Spectrosc. Relat. Phenom. **184**, 399 (2011).

[50] C. L. Perkins, M. Trenary, T. Tanaka, and S. Otani, X-ray photoelectron spectroscopy investigation of the initial oxygen adsorption sites on the LaB_6 (100) surface, Surf. Sci. **423**, L222 (1999).

[51] M. Belyansky and M. Trenary, Boron chemical shifts in B_6O, Surf. Sci. Spectra **3**, 147 (1995).

[52] N. Mannella, A. Rosenhahn, A. Nambu, B. C. Sell, B. S. Mun, S.-H. Yang,S. Marchesini, M. Watanabe, K. Ibrahim, S. B. Ritchey, Y. Tomioka, and C. S. Fadley, Surface characterization of colossal magnetoresistive manganites $La_{1-x}Sr_xMnO$ using photoelectron spectroscopy, J. Electron Spectrosc. Relat. Phenom. **153**, 37 (2006).

[53] A. M. Kaiser, A. X. Gray, G. Conti, B. Jalan, A. P. Kajdos, A. Gloskovskii, S. Ueda, Y. Yamashita, K. Kobayashi, W. Drube, S. Stemmer, and C. S. Fadley, Electronic structure of delta-doped La : $SrTiO_3$ layers by hard x-ray photoelectron spectroscopy, Appl. Phys. Lett. **100**, 261603 (2012).

[54] A. Kotani, M. Okada, T. Jo, A. Bianconi, A. Marcelli, and J. C. Parlebas, Many body effect in inner shell photoemission and photoabsorption spectra of La compounds, J. Phys. Soc. Jpn. **56**, 798 (1987).

[55] J. C. Fuggle, F. U. Hillebrecht, Z. Zołnierek, R. Lässer, Ch. Freiburg, O. Gunnarsson, and K. Schönhammer, Electronic structure of Ce and its intermetallic compounds, Phys. Rev. B **27**, 7330 (1983).

[56] S. Hüfner, *Photoelectron Spectroscopy, Principles and Applications*, 3rd ed. (Springer, Saarbrucken, 2003).

[57] F. de Groot and A. Kotani, *Core Level Spectroscopy of Solids* (CRC Press, New York, 2008).

[58] W.-Y. Howng and R. J. Thorn, The multicomponent structure of the 4d orbital in X-ray photoelectron spectra of the lanthanum(III) ion, Chem. Phys. Lett. **56**, 463 (1978).

[59] A Kotani and Y. Toyozawa, Photoelectron spectra of core electrons in metals with an incomplete shell, J. Phys. Soc. Jpn. **37**, 912 (1974).

[60] J. Zaanen, C. Westra, and G. A. Sawatzky, Determination of the electronic structure of transition-metal compounds: 2p x-ray photoemission spectroscopy of the nickel dihalides, Phys. Rev. B **33**, 8060 (1986).

[61] R. D. Cowan, *The Theory of Atomic Structure and Spectra* (University of California Press, Berkeley, 1981).

[62] M. W. Haverkort, Quanty for core level spectroscopy - excitons, resonances and band excitations in time and frequency domain, J. Phys. Conf. Ser. **712**, 012001 (2016).

[63] Y. Kayanuma, in *Hard X-ray Photoelectron Spectroscopy (HAXPES)*, edited by J. Woicik, (Springer, New York, 2016), Vol. 8, pp. 175–195.

[64] S. Suga, A. Sekiyama, H. Fujiwara, Y. Nakatsu, T. Miyamachi, S. Imada, P. Baltzer, S. Niitaka, H. Takagi, K. Yoshimura, M. Yabashi, K. Tamasaku, A. Higashiya, and T. Ishikawa, Do all nuclei recoil on photoemission in compounds? New J. Phys. **11**, 073025 (2009).

[65] C. P. Flynn, Phonon Broadening of Deep Excitations in Metals, Phys. Rev. Lett. **37**, 1445 (1976).

[66] W. Domcke and L. Cederbaum, Electronic recoil effects in high-energy photoelectron spectroscopy, J. Electron Spectrosc. Relat. Phenom. **13**, 161 (1978).

[67] Y. Takata, Y. Kayanuma, M. Yabashi, K. Tamasaku, Y. Nishino, D. Miwa, Y. Harada, K. Horiba, S. Shin, S. Tanaka, E. Ikenaga, K. Kobayashi, Y. Senba, H. Ohashi, and T. Ishikawa, Recoil effects of photoelectrons in a solid, Phys. Rev. B **75**, 233404 (2007).

[68] Y. Takata, Y. Kayanuma, S. Oshima, S. Tanaka, M. Yabashi, K. Tamasaku, Y. Nishino, M. Matsunami, R. Eguchi, A. Chainani,

M. Oura, T. Takeuchi, Y. Senba, H. Ohashi, S. Shin, and T. Ishikawa, Recoil Effect of Photoelectrons in The Fermi Edge of Simple Metals, Phys. Rev. Lett. **101**, 137601 (2008).

[69] Z. Boekelheide, A. X. Gray, C. Papp, B. Balke, D. A. Stewart, S. Ueda, K. Kobayashi, F. Hellman, and C. S. Fadley, Band Gap and Electronic Structure of an Epitaxial, Semiconducting $Cr_{0.80}Al_{0.20}$ Thin Film, Phys. Rev. Lett. **105**, 236404 (2010).

[70] D. A. Shirley, High-resolution x-ray photoemission spectrum of the valence bands of gold, Phys. Rev. B **5**, 4709 (1972).

[71] M. M. Korsukova, T. Lundstrom, L.-E. Tergenius, and V. N. Gurin, The X-ray debye temperature of LaB_6, Solid State Commun. **63**, 187 (1987).

[72] C. S. Fadley, Looking deeper: Angle-resolved photoemission with soft and hard X-rays, Synchrotron Radiat. News **25**, 26 (2012).

[73] A. X. Gray, J. Minár, S. Ueda, P. R. Stone, Y. Yamashita, J. Fujii, J. Braun, L. Plucinski, C. M. Schneider, G. Panaccione, H. Ebert, O. D. Dubon, K. Kobayashi, and C. S. Fadley, Bulk electronic structure of the dilute magnetic semiconductor $Ga_{1-x}Mn_xAs$ through hard X-ray angle-resolved photoemission, Nat. Mater. **11**, 957 (2012).

[74] C. Papp, L. Plucinski, J. Minár, J. Braun, H. Ebert, C. M. Schneider, and C. S. Fadley, Band mapping in x-ray photoelectron spectroscopy: An experimental and theoretical study of W(110) with 1.25 keV excitation, Phys. Rev. B **84**, 045433 (2011).

[75] X. Guo-Liang, C. Jing-Dong, X. Yao-Zheng, L. Xue-Feng, L. Yu-Fang, and Z. Xian-Zhou, First-principles calculations of elastic and thermal properties of lanthanum hexaboride, Chin. Phys. Lett. **26**, 056201 (2009).

[76] D. Liebowitz and N. J. Shevchik, Free-electron final-state model and angle-resolved photoemission from a Ag(111) surface, Phys. Rev. B **17**, 3825 (1978).

[77] L. Plucinski, J. Minár, B. C. Sell, J. Braun, H. Ebert, C. M. Schneider, and C. S. Fadley, Band mapping in higher-energy X-ray photoemission: Phonon effects and comparison to one step theory, Phys. Rev. B **78**, 035108 (2008).

[78] J. Minár, J. Braun, and H. Ebert, Recent developments in the theory of HARPES, J. Electron. Spectrosc. Relat. Phenom. **190**, 159 (2013).

[79] A. Hasegawa and A. Yanase, Energy band structure and Fermi surface of LaB, by a self-consistent APW method, J. Phys. F: Metal Phys. **7**, 1245 (1977).